Predictive Thermal Modeling and Characterization of Ultrasonic Consolidation Process for Thermoplastic Composites

Madeline Kirby
Department of Mechanical and Industrial Engineering,
Louisiana State University,
Baton Rouge, LA 70803
e-mail: madeline.k.kirby@boeing.com

Armaghan Naderi
Department of Mechanical and Industrial Engineering,
Louisiana State University,
Baton Rouge, LA 70803
e-mail: anader2@lsu.edu

Genevieve Palardy[1]
Department of Mechanical and Industrial Engineering,
Louisiana State University,
Baton Rouge, LA 70803
e-mail: gpalardy@lsu.edu

Ultrasonic consolidation (USC) of thermoplastic composites is a highly attractive and promising method to manufacture high-performance composites. This work focuses on USC of dry carbon fiber (CF) fabrics with high-temperature polyphenylene sulfide (PPS) films. Experimental trials to assess feasibility of the process are time-consuming. Consequently, a predictive thermal model would facilitate process parameters selection to reduce expensive trial-and-error approaches. This paper presents a 2D finite element model of samples under consolidation, incorporating equations for viscoelastic heating, matrix phase change, and material properties. Theoretical temperature profiles for nodes of interest were compared to the corresponding experimental temperature curves for various control parameters (i.e., weld time and vertical displacement of sonotrode) and showed good agreement during heating phase. It was found that welding time values below 1750 ms were insufficient to reach melting temperature, whereas weld times above 3000 ms led to the lowest average void content (2.43 ± 0.81%). More specifically, the time the material spent above melting temperature, i.e., residence time, was established as a parameter that could estimate cases resulting in better consolidation and lower void content (time above 2600 ms for void content below 2.5%). X-ray diffraction (XRD) characterization revealed that the USC process led to mostly amorphous PPS, due to the high cooling rates (70 °C/s to 108 °C/s). Overall, the thermal model and micro-structural outcomes confirmed the feasibility of the USC process for layered composites made from dry fabric and high-temperature thermoplastic films. [DOI: 10.1115/1.4056147]

Keywords: ultrasonic consolidation, thermoplastic composites, carbon fiber, viscoelastic heat generation, advanced materials and processing, welding and joining

1 Introduction

The modern expansion and technological evolution of the aerospace and automotive industries has increased the demand for high-quality and cost-effective manufacturing processes for lightweight composite structures. Thermoplastic composites (TPCs) are highly compatible with this demand, as they require shorter manufacturing times and can be re-heated for molding and forming, as well as assembled through fusion bonding (i.e., welding) [1]. Ultrasonic consolidation (USC) of TPCs is a promising high-speed manufacturing method, providing energy efficiency and ease of automation. It utilizes ultrasonic vibrations and pressure applied by a horn (or sonotrode) to generate frictional and viscoelastic heating between material layers, thereby melting the thermoplastic matrix and infusing the fibers to produce semi-finished parts. So far, its feasibility has been demonstrated for consolidation of TPC prepregs, rovings, and dry fibers.

While the analogous process of ultrasonic welding has been utilized since the 1980s [1], research as it pertains to thermoplastic composite parts has only been conducted in depth for just under a decade. This includes experimental studies on weld quality and failure modes in spot welds for short fiber composites [2–4], process monitoring through output data [5], liquid thermoplastic composites joining [6], as well as continuous welding for long seams [7,8]. Numerical studies to predict heat generation have been performed to investigate contact behavior at the interface [9] and to assess temperature rise through a multi-timescale framework [10]. However, those studies are related to the welding process between pre-fabricated adherends, and there have been very few studies on USC of TPCs from raw materials to finished parts. In particular, Rizzolo and Walczyk tested the use of ultrasonic heating for automated fiber placement (AFP) of unidirectional (UD) glass fiber (GF)/high-density polyethylene and UD carbon fiber (CF)/polyethylene terephthalate (PET) tapes [11]. Their aim was to replace traditional AFP heating methods, such as hot gas, infrared, and laser heating. They accomplished this by placing tapes onto a moving stage under a stationary sonotrode, and by manufacturing UD and quasi-isotropic layups. They demonstrated that the strength and stiffness of the layups were lower than compression molded laminates, except for CF/PET. A simplified heat generation model, based on surface energy pulse, was proposed to predict temperature trends between plies, but it showed differences by at least 30 °C with experimental thermocouple data. Moreover, micro-structural quality was not investigated at that stage. Gomer et al. conducted an extensive study on USC of dry CF and GF with polyamide 6 (PA6), polyethylene, and polypropylene (PP) films [12]. They successfully demonstrated the feasibility of this method by stacking thermoplastic film and dry fiber layers, then applying ultrasonic vibrations in a single spot or continuously through a rolling sonotrode. They reported tensile strengths up to 1.2 GPa and a maximum fiber volume fraction of 33% for CF/PA6 samples. While multiple combinations of materials were experimentally studied, several characteristics were not yet investigated in detail, including micro-structural quality, porosity, heat generation, and matrix crystallization behavior.

Lionetto et al. [13,14] demonstrated the use of USC for commingled rovings (GF and PP filaments) on a rotating mandrel. The process produced samples with density and storage shear modulus

---

[1] Corresponding author.

Manuscript received June 1, 2022; final manuscript received October 24, 2022; published online December 5, 2022. Assoc. Editor: Martine Dubé.

values falling within typical range for compression molded samples. However, the void content was slightly higher (1.8% versus 1.9–4.6%). A 2D finite element (FE) model was developed with COMSOL MULTIPHYSICS to predict temperature distribution during USC of rovings, taking into consideration ultrasonic heat generation and power required to melt the PP matrix. A moving mesh module was implemented to simulate the roving speed when rotating on the mandrel. Comparison between experimental and numerical results showed good agreement in terms of peak temperature. Dell'Anna et al. expanded upon their previous work by investigating USC of semi-preg UD GF/LPET (amorphous poly(ethylene terephthalate)) tapes through physical, mechanical and, micro-structural characterization for various winding speeds [15]. Winding speed did not present any clear trend for density, void content (between 1.7% and 3.2%), or storage shear modulus, but nonetheless, the reliability of this manufacturing method was demonstrated for this type of UD tape. Overall, research gaps were identified in the literature regarding USC of TPCs. First, high-temperature, high-performance thermoplastic matrices have not been investigated (e.g., polyether ether ketone, polyphenylene sulfide (PPS), or polyether imide). It is assumed that the higher melting temperatures to consolidate such matrices would require significantly more power from the welder, possibly limiting its use. Second, most experimental studies are focused on UD fiber composites. Woven fabrics present additional challenges [16], for which micro-structural quality has not been explored experimentally with respect to USC. Finally, there is a lack of comprehensive thermal models for this process, including experimental validation at various locations across the samples. Prediction of temperature profile throughout specimens is valuable as it affects matrix melting, fiber impregnation, and recrystallization behavior, and thus, quality of the final laminate.

Therefore, the current study focuses on USC of dry CF fabric layers with high-temperature PPS films. While previous work demonstrated feasibility of this process under a range of welding forces [17], experimental trials are time-consuming. Consequently, a predictive thermal model would facilitate process parameters selection to reduce expensive trial-and-error campaigns. This paper's main goal is two-fold: (1) develop a simplified FE model to predict temperature profile for CF/PPS samples with experimental validation and (2) further understand the effect of ultrasonic control parameters (vertical sonotrode displacement or weld time) on micro-structural quality to provide process guidelines based on thermal history. This paper will first present the implementation of a predictive 2D FE model for the cross-sectional temperature distribution of samples under consolidation, using the MATLAB partial differential equations (PDE) solver. Theoretical temperature profiles for various welding parameters are then compared to the corresponding experimental temperature values to assess the model's accuracy. Finally, consolidated samples are characterized for void content and matrix crystalline structure through micro-computed tomography (μCT) and X-ray diffraction (XRD), respectively.

2 Experimental Methods

2.1 Materials. This study used Natural Fortron® PPS films (SKX-382, purchased from Professional Plastics, CA) with a thickness of 0.08 mm and Toray T-300 standard modulus CF 3k twill weave fabric (purchased from Composite Envisions, WI). The CF fabric had an areal density of 267 gsm. All sheets were pre-cut into 50 mm × 50 mm layers.

2.2 Ultrasonic Consolidation. A Rinco Ultrasonics Dynamic 3000 ultrasonic welder with a 40 mm-diameter cylindrical sonotrode was used to consolidate the CF and PPS layers at a frequency of 20 kHz up to a maximum power of 3000 W. The vibrational amplitude was set to 38.1 μm and a consolidation force of 1000 N was used for all trials. Solidification force and holding time were set to 1000 N and 2000 ms, respectively. The welding and solidification force correspond to a pressure of approximately 0.8 MPa, which is in line with a typical pressure range applied during compression molding of CF/PPS prepregs (0.7–2.0 MPa, as specified by manufacturer's data sheet). The main process steps are shown in Fig. 1, along with ply stacking sequence, which consists of three CF layers between four PPS films in 0 deg orientation with a layer of polyimide film (Kapton®, American Durafilm, Holliston, MA) between the topmost PPS layer and the sonotrode face. Welding parameters and number of layers were selected based on preliminary results from a previous study, showing the effect of welding force and vertical sonotrode displacement on consolidation quality [17]. Sample size was sufficient to display representative behavior of the process under a single consolidation step [12]. The welding process was controlled in two ways: (1) downward vertical displacement of the sonotrode (also referred to as "travel") and (2) vibration duration (weld time). Four travel values were considered: 0.11 mm, 0.15 mm, 0.20 mm, and 0.25 mm, based on preliminary trials producing consistent outputs.

To further assess the effect of control parameters on temperature profile and to confirm the predictive capabilities of the theoretical model, four vibration times were also selected to obtain experimental measurements during USC: 1000 ms, 1750 ms, 2500 ms, and 3250 ms. After consolidation, the welder provided four primary outputs, in addition to its power and displacement curves: weld time (ms), energy (J), maximum power (%), and weld distance (mm). In both control modes, weld time is the primary input for the theoretical model.

2.3 Compression Molding of Dry Carbon Fiber Plies. To create reference specimens, CF/PPS laminates were compression

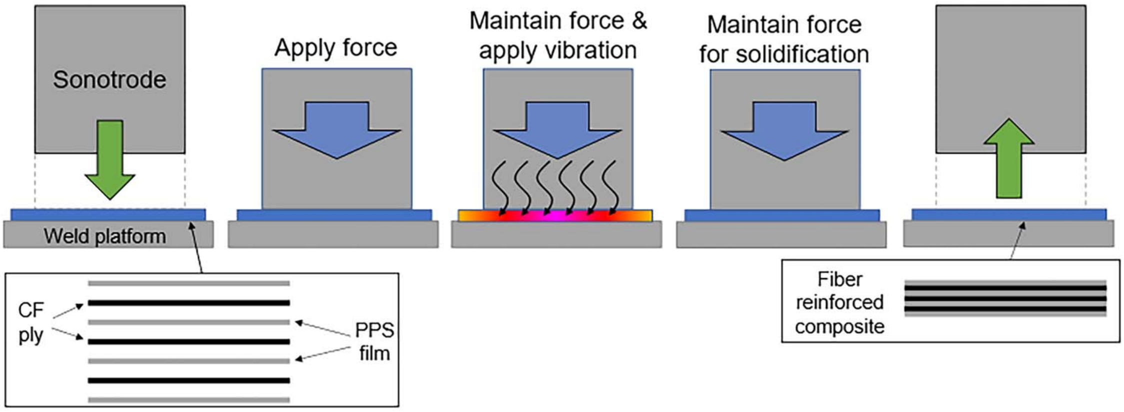

Fig. 1 **Schematic illustration of steps in the USC process for creating fiber-reinforced CF/PPS composite samples**

molded using dry CF plies and PPS films in the same stacking sequence as shown in Fig. 1. Samples were placed in a heated press (Dake, 75 ton) and consolidated at 320 °C at approximately 0.8 MPa pressure for 20 min, then cooled in the press under pressure. Those samples possessed a nominal thickness approximately equal to 0.7 mm, with an estimated fiber volume fraction of 50%. Void content was compared with ultrasonically consolidated specimens using optical microscopy. Samples were cut and mounted in an epoxy mold. They were grinded with 180, 360, 600, 800, and 1200 grit SiC abrasive pads, and then polished with 6 and 1 μm diamond solutions.

2.4 Temperature Measurements. To validate the theoretical temperature profiles, direct thermocouple (TC) measurements between plies were acquired, as illustrated in Fig. 2. K-type thermocouples (36 American wire gauge (AWG) purchased from Omega Engineering, Norwalk, CT) were stripped and placed in three locations throughout the sample (N1, N2, and N3) and taped flush to the platform, ensuring minimal interference with the perceived thickness of the sample. It is to be noted that the insertion of more than three thermocouples created issues with the welding process as their total thickness affected the compaction and flow of the stacked plies. Thermocouples were connected to a PC through a Model DI-2008 Thermocouple and Voltage data acquisition (DAQ) and Data Logger System in order to store temperature data. Measurements were taken at a sampling rate of 67 samples per second.

2.5 Void Content Characterization. Void content of the ultrasonically consolidated travel-based samples was characterized with a desktop cone-beam μCT scanner (Scanco Model 40, Switzerland). Specimens for the four trials were cut into 10 mm × 10 mm segments from the center of each consolidated sample, but away from any embedded TCs to avoid possible disturbance. 3D reconstruction was performed with AVIZO software from Thermo Fisher Scientific. Over ten DICOM slices were taken from each scan and analyzed with IMAGEJ software (version 1.8.0, National Institutes of Health) brightness thresholding to determine average void content for each sample. It is to be noted that frayed edges were observed in some cases, which were not considered in the overall void content assessment.

2.6 X-Ray Diffraction Analysis for Crystalline Structure. The crystalline structure of PPS films and ultrasonically consolidated CF/PPS samples was studied by X-ray diffractometer (PANalytical Empyrean, United Kingdom) over a 2θ range of 5–80 deg for solid samples. Two types of PPS film samples were investigated: (i) as received (labeled "AS_R") and (ii) after USC (four-layer stack under 1000 N, 38.1 μm amplitude, and 0.2 mm travel). They were characterized to assess if the process affected the crystalline structure. The latter case (four-layer PPS stack) and CF/PPS samples were cut out as shown in Fig. 3. The XRD settings were continuous CuKα radiation ($\lambda = 0.1540598$ nm) with a step size of 0.02 deg, generator voltage of 45 kV, and tube current of 40 mA. It is to be noted that differential scanning calorimetry (DSC) was used in a previous study to quantify crystallinity of pure PPS films (before welding) and after ultrasonic consolidation with CF layers [17]. The average crystallinity of pure PPS films was approximately equal to 25%, which is comparable to other studies in the literature with values between 22% and 26% [18,19]. For the ultrasonically consolidated CF/PPS samples, it proved difficult to isolate the PPS films as they were embedded into the woven fabric, leading to large scatter in the data. This was also observed by Koutras et al. [19] for PPS films used for ultrasonic welding of CF/PPS laminates due to non-uniform crystallization during cooling. Therefore, XRD was selected to assess the effect of USC on PPS diffractograms as they provide a relative order of magnitude between the samples for comparison purposes.

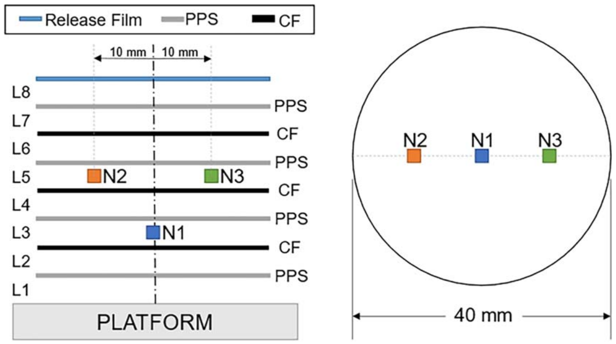

Fig. 2 Ply stacking sequence with in situ thermocouple layout (left) and top view of thermocouple layout (right)

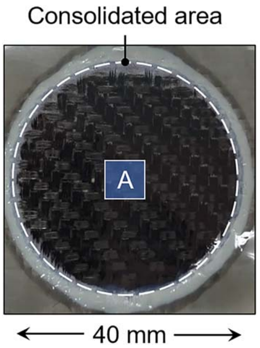

Fig. 3 Top view of consolidated CF/PPS sample with surface areas used for XRD (A: top and bottom). The same areas were used for XRD experiments of the four-layer PPS stack after USC.

3 Theoretical Model

A MATLAB program was written to generate a theoretical cross-sectional temperature profile over the weld area throughout ultrasonic consolidation and cooling. Figure 4 shows the flow logic diagram for the code. The general form of the heat equation is given by the two-dimensional (2D) heat equation with heat generation H via viscoelastic heating Q (heat source) and melting energy of the PPS matrix $\dot{H}_m$ (heat sink), as shown in Eq. (1) [13]:

$$k\frac{\partial^2 T}{\partial x^2} + k\frac{\partial^2 T}{\partial y^2} + H = \rho C_p \frac{\partial T}{\partial t} \tag{1}$$

where k is the thermal conductivity, ρ is the density, C_p is the specific heat, and H is given by Eq. (2):

$$H = Q - \rho \dot{H}_m \tag{2}$$

Utilizing the PDE Toolbox's Heat Transfer utility, the viscoelastic heating, melting heat, and material properties were applied to the general form of the heat equation with temperature dependence. The program is written to solve for the temperature gradient over the mesh at each time-step until the simulation time reaches the user-specified value. For its first iteration, the program uses the specified initial value for ambient temperature and takes the initial heat generation and time equal to zero. The initial material properties are also taken at ambient temperature (obtained from suppliers' data sheets and literature [13,20,21]). Over the first step, the value of H is updated to reflect the initiation of the welding process based on the state of heat generation in the welding cycle. The PDE solver takes H, ρ, C_p, and k as inputs and calculates the new nodal temperatures over the meshed area for the given time-step. These temperatures are used as the initial temperatures in the following time-step, giving updated values for $H(T)$, $\rho(T)$, $C_p(T)$, and $k(T)$, and the calculation is run again, storing the nodal temperatures each time. This process

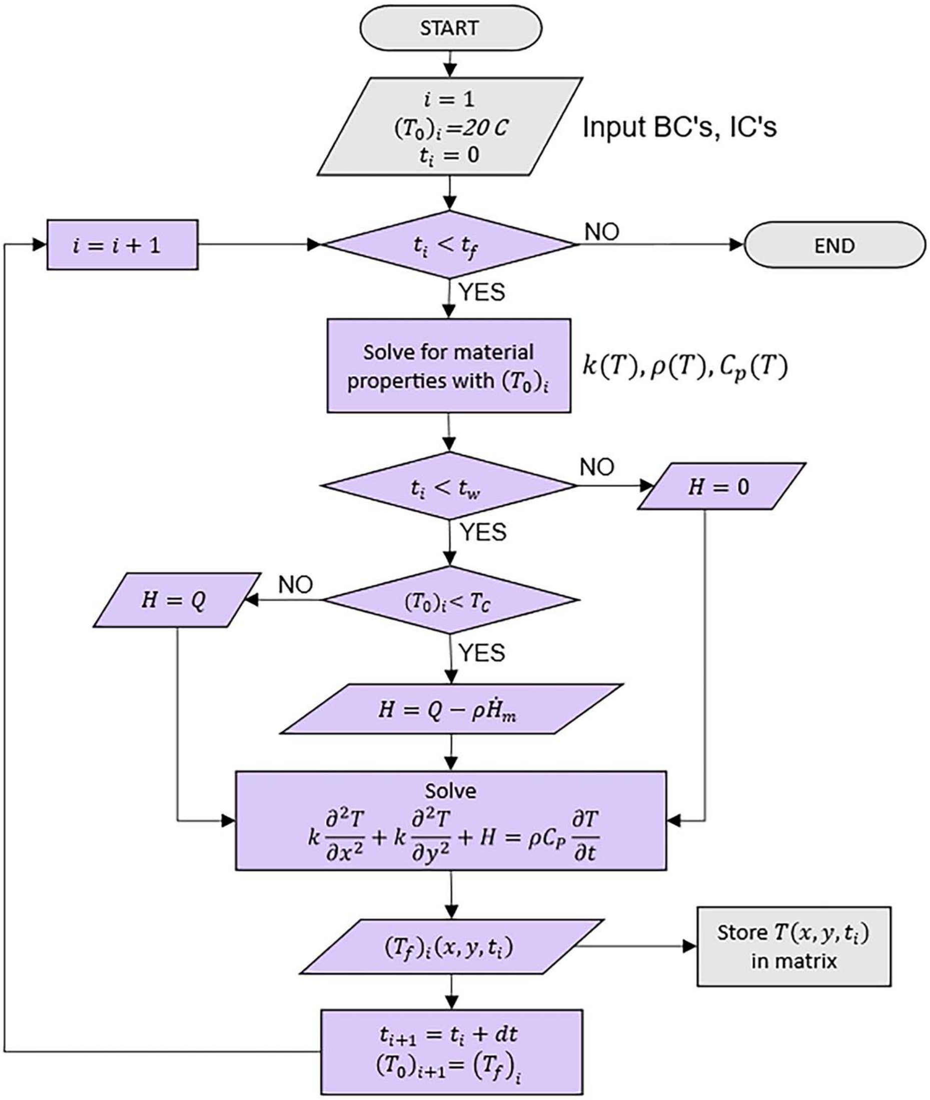

Fig. 4 Flow logic diagram for code, starting from input BCs and initial conditions

repeats until the sum of the time-steps reaches the user-defined limit $t_{\lim}$ (based on weld times used to control the USC process or obtained as outputs after the process, as described in Sec. 2.2). The program outputs a 2D temperature gradient for each time-step over a given consolidation cycle.

3.1 Viscoelastic Heating.

For this model, viscoelastic heating was considered as the main heat generation mechanism, similarly to ultrasonic impregnation proposed in the literature [13]. The heat generation term Q represents the applied vibrational energy being dissipated as heat through intermolecular friction, i.e., viscoelastic heating. Q depends on the applied frequency ω, the square of strain amplitude ε_0 of the ultrasonic vibration, and the loss modulus of the material E'' as shown in Eq. (3) [22]:

$$Q = \alpha \frac{\omega \varepsilon_0^2 E''}{2} \tag{3}$$

The factor α is a lumped, efficiency parameter that represents any losses from the translation of vibrational energy to heat (i.e., hammering, generator efficiency, acoustic losses, energy dissipation in specimen, and clamping fixture) [23]. To capture thermal behavior, this factor was determined to be 0.15 based on the literature [24] and comparison between theoretical and measured data points for several sets of weld parameters [25].

The loss modulus E'' for the PPS film was measured using a dynamic mechanical analyzer (TA Instruments Q800 DMA) apparatus from ambient temperature to 160 °C at frequencies of 0.1, 1, 10, and 100 Hz. Film specimens were cut into 18 mm × 8 mm rectangular samples and clamped with a torque of 0.34 N m between the tensile fixture of the DMA. Using the time-temperature superposition method described by Levy et al. [23], the data were shifted to the 1 Hz master curve to obtain a shift factor that can be used to extrapolate to 20 kHz. With this technique, a temperature shift factor of −24.02 °C was obtained for 20 kHz, yielding $E'' =$ 0.028 GPa at room temperature. For this model, E'' is held constant at this value for all temperatures. The strain amplitude ε_0 was determined based on a model from Ref. [26] stating that ε_0 is a function of the ratio of the moduli of the matrix and fiber layers. This method led to $\varepsilon_0 = 0.0127$ for this configuration.

3.2 Melting Heat.

The heat required to melt the PPS matrix $\dot{H}_m$ is a function of the degree of melting X_m as shown in Eq. (4):

$$\dot{H}_m = H_T \frac{dX_m}{dt} \tag{4}$$

where H_T is a reference value representing the total heat absorbed throughout the entire heating process, given by Eq. (5):

$$H_T = \int_{T_i}^{T_f} dH^* dT \tag{5}$$

The degree of melting is defined by Eq. (6):

$$X_m(T) = \frac{H(T)}{H_T} \tag{6}$$

X_m can be expressed by the statistical approach of Greco and Maffezzoli [27] based on the assumption that the melting peak, obtained through DSC, can be regarded as a statistical distribution of melting temperatures resulting from a distribution of lamellar thicknesses also known as the Richards function [28,29]. This relation depends on the temperature at the peak of the DSC signal, T_C, an intensity factor k_{mb}, and a shape factor d. For simplicity, an alternative form of Richards equation from Ref. [30] was used, given by Eq. (7):

$$X_m(T) = \frac{X_{m,\max}}{[1 + de^{-k_{mb}(T-T_C)}]^{1/d}} \tag{7}$$

where

$$\frac{dX_m}{dT} = X_{m,\max} \frac{k_{mb} e^{(-k_{mb}(T-T_c))}}{[1 + de^{-k_{mb}(T-T_C)}]^{(1/d)+1}} \tag{8}$$

where $X_{m,\max}$ is the maximum value calculated using DSC data points. MATLAB's curve fitting tool was used to obtain a fit to the DSC data with $R^2 = 0.9963$ and 95% confidence interval. The parameters were assigned the corresponding values: $d = 0.6566$ and $k_{mb} = 9.428$. The fit and its derivative were plotted against experimental data (Fig. 5) for the range of measured temperatures.

The MATLAB PDE Solver was provided with a conditional statement that would set the heat sink term $\dot{H}_m = 0$ once the temperature reached $T_C = 291.1\,^\circ\mathrm{C} = 564.2$ K (corresponding to $X_m = 1$). The heat source term can be represented by the following piecewise function in Eq. (9):

$$H(T) = \begin{cases} Q - \rho(T)\dot{H}_m(T), & T \le T_C \\ Q, & T > T_C \end{cases} \tag{9}$$

As shown in Eq. (10), a second conditional statement was set to assign the heat generation term $H = 0$ once t_{weld} is achieved:

$$H = \begin{cases} H(T), & 0 \le t \le t_{\mathrm{weld}} \\ 0, & t > t_{\mathrm{weld}} \end{cases} \tag{10}$$

3.3 Material Properties.

To determine the composite material properties, a few assumptions were made for the simplified FE model implementation. The rule of mixtures was used with constituent properties shown in Table 1. To account for phase change, "dry" and "wet" states were introduced through the rule of mixtures in Eqs. (11)–(14) for specific heat C_p and thermal conductivity k [14]:

$$k_{\mathrm{dry}} = k_{\mathrm{pps}}\Phi_{\mathrm{pps}} + k_{\mathrm{CF}}\Phi_{\mathrm{CF}} + k_{\mathrm{air}}\Phi_{\mathrm{air}} \tag{11}$$

$$C_{p\mathrm{dry}} = C_{p\mathrm{pps}}\Phi_{\mathrm{pps}} + C_{p\mathrm{CF}}\Phi_{\mathrm{CF}} + C_{p\mathrm{air}}\Phi_{\mathrm{air}} \tag{12}$$

$$k_{\mathrm{wet}} = k_{\mathrm{pps}}\Phi_{\mathrm{pps}} + k_{\mathrm{CF}}\Phi_{\mathrm{CF}} \tag{13}$$

$$C_{p\mathrm{wet}} = C_{p\mathrm{pps}}\Phi_{\mathrm{pps}} + C_{p\mathrm{CF}}\Phi_{\mathrm{CF}} \tag{14}$$

where Φ_{pps}, Φ_{CF}, and Φ_{air} represent the volume fraction of PPS, carbon fiber, and air, respectively, and Φ_{air} is assumed to be 30%. The volume fractions were calculated using the overall volume of the dry constituents with $\Phi_{\mathrm{CF}} = 0.5769$ and $\Phi_{\mathrm{pps}} = 0.1758$. The composite specific heat C_p and thermal conductivity k along with matrix density ρ_m were calculated using the rule of mixtures, which was assumed to represent material behavior for the FE model, where X_m is the percentage of the material in the melted or "wet" phase, given by Eqs. (15)–(17) [14]:

$$k = k_{\mathrm{dry}}(1 - X_m(T)) + k_{\mathrm{wet}}X_m(T) \tag{15}$$

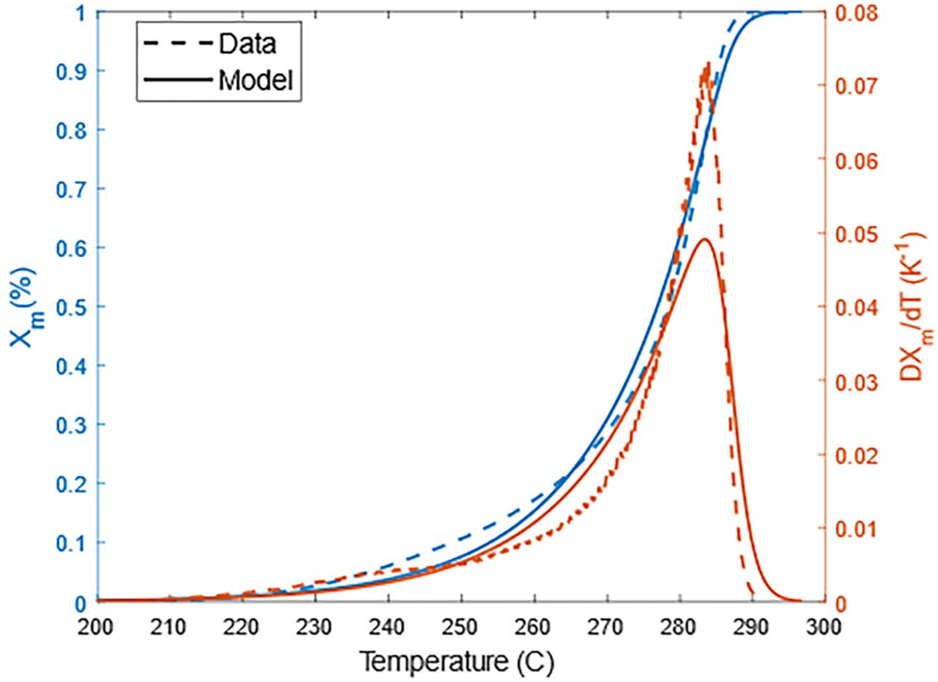

Fig. 5 Measured data from DSC and curve-fit for PPS matrix degree of melting, X_m, and dX_m/dT

Table 1 Sonotrode and welding platform material properties (obtained from suppliers' data sheets and literature [13,20,21])

	Sonotrode (titanium)	Welding platform (stainless steel)	Carbon fiber	PPS film Liquid	PPS film Solid	Air
ρ (kg/m^3)	4507	7860	1760	1264	1082	
k (W/mK)	18	15	10.46	0.30		0.026
C_p (J/kg K)	544	502	717	2000		1005

$$C_p = C_{p\text{dry}}\ (1 - X_m(T)) + C_{p\text{wet}} X_m(T) \tag{16}$$

$$\rho_m = (\rho_m)_{\text{dry}}(1 - X_m(T)) + (\rho_m)_{\text{wet}} X_m(T) \tag{17}$$

Equations (15)–(17) generally captured the behavior for each property with respect to $X_m(T)$. During consolidation, a portion of the generated heat is conducted to the sonotrode and welding platform through direct contact. Since the PDE toolbox cannot discern surface contact, the heat generation term was specified as a volumetric heat source within the composite that directly contacts the sonotrode face and welding platform with material properties listed in Table 1. All faces contacting open air were prescribed a boundary condition (BC) of free convection at $T_\infty = 20\,°\text{C} = 293.15\,\text{K}$ with $h = 5$ W/mK. Adiabatic conditions were assumed at all other boundaries. This limitation also prohibits direct representation of the loss of contact between the sonotrode and the sample after the vibration phase is completed. To address this, the material properties of the sonotrode were changed to those of air following the holding time to represent the sonotrode lifting following ultrasonic consolidation.

3.4 Model Description. As shown in Fig. 6, the cross-sectional geometry of the weld platform (F1), sample (F2, F3, and F4), and sonotrode (F5) were specified as independent geometries with distinct material properties. The coordinate system is centered on the sample and all face dimensions can be found in Table 2. The dimensions of F1 and height of F5 were chosen to sufficiently capture the conduction into each component from the heat source. The overall height of the sample (1.8 mm) was calculated using the combined pre-consolidated thicknesses of the CF and PPS layers. The sample was segmented into three parts, with F2 and F3 representing the outer perimeter that would remain unconsolidated, and F4 representing the projected area of the sonotrode in direct contact with the sample. The heat generation term H is applied to F4 as a volumetric heat source. A quadratic mesh was generated over the entire shape shown in Fig. 6 with element size $0.0021 < s < 0.0043$ and mesh gradation of 1.5.

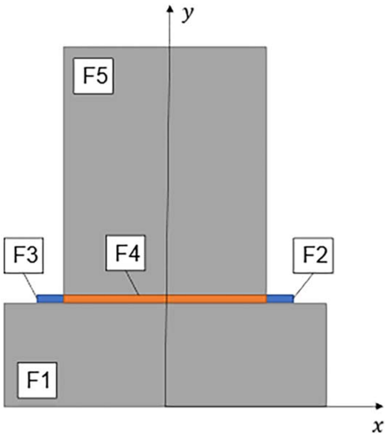

Fig. 6 Geometry layout for heat generation model. See Table 2 for description of each component.

For a given time-step size, the program iteratively saves nodal temperatures in a matrix over the simulation time, which are then plotted to a 2D heatmap for visualization. The user may input an overall simulation time greater than the weld time to observe the sample cooling after consolidation is complete. Temperature curves can be extracted at coordinates of interest for comparison to experimental temperature data.

4 Results and Discussion

4.1 Heat Generation: Modeling and Experimental Results. The FE model provides the temperature profile throughout the specimen during matrix melting, consolidation, and cooling. Having the ability to predict the temperature distribution in the composite is highly valuable, as it strongly affects impregnation and recrystallization, and therefore, quality of the final laminate. Several cases were considered for simulations and a representative example of the 2D temperature distribution at different time values (t) is shown in Fig. 7 for a full weld cycle (sample consolidated under 1000 N and a travel of 0.20 mm). During the welding process (from Figs. 7(*b*) and 7(*c*)), the centerline (axial) temperature of the specimen exceeds the melting temperature of the PPS matrix (above 280 °C) in the mid-plane of the sample. The temperature continues to increase until the sonotrode vibration is switched off (Fig. 7(*c*)) and maintains a normal force of 1000 N for an additional 2 s. The sonotrode is then lifted (Fig. 7(*d*)), allowing the specimen to further cool down until the simulation concludes (10 s).

To assess agreement between predictive model and experiments, ultrasonic consolidation was conducted in two sets, as listed in Table 3: the first with sonotrode travel as the control parameter (trials 1–4) and the second with weld time as the control parameter (trials 5–8). The temperature profiles were measured with K-type thermocouples approximately placed at three nodes of interest (as shown in Fig. 2) to assess the effect of position and the experimental variability. Welder output values (weld time, weld distance, energy and maximum power) are summarized in Table 3 for each trial. It is to be noted that the weld time in trial 1 (0.11 mm travel) is higher than that of trials 2 and 3. This discrepancy is likely due to inconsistencies in the perceived downward displacement of the machine. For very low travel values (<0.10 mm), it was observed that the welder would often execute the maximum allowable weld time (10 s), leading to an incomplete welding procedure. To maintain a data point for a low desired travel, the first trial was designated a travel value of 0.11 mm, but still exhibited higher weld time than

Table 2 Two-dimensional FE model geometry dimensions

Representative component		(*F*#)	Width (mm)	Height (mm)
Weld platform		1	75	25
Sample	Unconsolidated	2,3	5	1.8
	Consolidated	4	40	1.8
Sonotrode		5	40	50

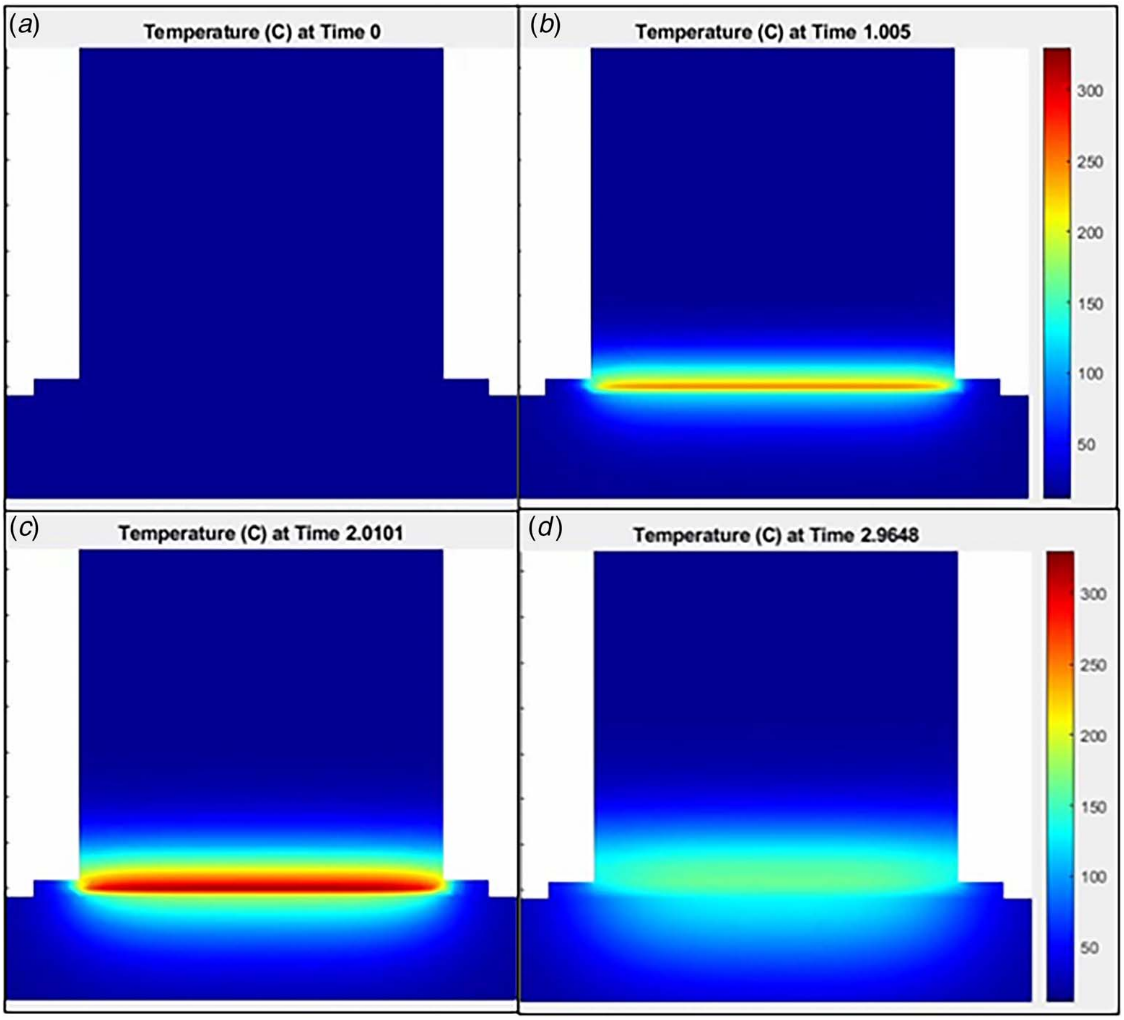

Fig. 7 Temperature gradient progression at different time values (in seconds) for welding conditions of 1000 N and 0.20 mm travel: (*a*) before weld, (*b*) during weld, (*c*) at peak temperature (end of weld), and (*d*) post-weld cooling (solidification phase)

expected. It is assumed that the presence of thermocouples throughout the samples may have affected the perceived travel, as the wires thickness is on the same order of magnitude as the overall travel (~0.12 mm).

Simulation results were compared with experiments for all trials listed in Table 3. It is worth mentioning that the FE simulations for the travel-control trials (1–4) were carried out after the experiments took place, as the weld time is governed by the final vertical displacement of the sonotrode (i.e., weld distance in Table 3). For the corresponding simulations, time was employed as the input parameter. Temperature profiles at coordinates corresponding to each thermocouple node were extracted from the FE model and plotted with experimental data for trials 1–4 (Fig. 8). Horizontal lines corresponding to "total melting" of the PPS matrix ($X_m = 1$ at T_C) are denoted on each plot. For all cases, nodal temperatures met and exceeded the melting temperature of the PPS matrix except for node 1 in the 0.11 mm case, which read a peak temperature of approximately 278 °C at 2386 ms. In fact, peak temperatures at node 1 for all cases are the lowest of the three nodes. Since the thermocouple placed at node 1 is closer to the platform than nodes 2 and 3 (Fig. 1), it is possibly less affected by the heat generated at the sonotrode interface and therefore experiences a smaller rise in temperature. This behavior was also reported for ultrasonic consolidation of thermoset prepregs similar to automatic fiber placement [31], including repair applications [32]. The FE model has potential to capture this behavior as the heat generation is volumetric within the sample geometry.

In general, higher travel values (and therefore longer weld times) resulted in higher measured peak temperatures at each node for the travel-control trials. Good agreement between experiments and modeled temperature profiles in the heating phase is observed until peak temperature is observed (Fig. 8), except for node 1 and node 2 for the 0.25 mm case. Differences such as these are likely caused

Table 3 Travel, weld time, weld distance, energy consumption, and maximum power for main experimental trials

Trial #	Travel (mm)	Weld time (ms)	Weld distance[a] (mm)	Energy (J)	Max. power (%)
1	0.11[b]	2386	0.19	2794	44
2	0.15[b]	1903	0.24	2250	43
3	0.20[b]	2147	0.28	2593	44
4	0.25[b]	3814	0.28	4370	43
5	–	1000[b]	0.26	1123	44
6	–	1750[b]	0.25	2056	44
7	–	2500[b]	0.27	2939	43
8	–	3250[b]	0.30	3790	43

[a] The final travel value provided by the welder at the end of the 2 s holding phase.

[b] Indicates input value used on the welder.

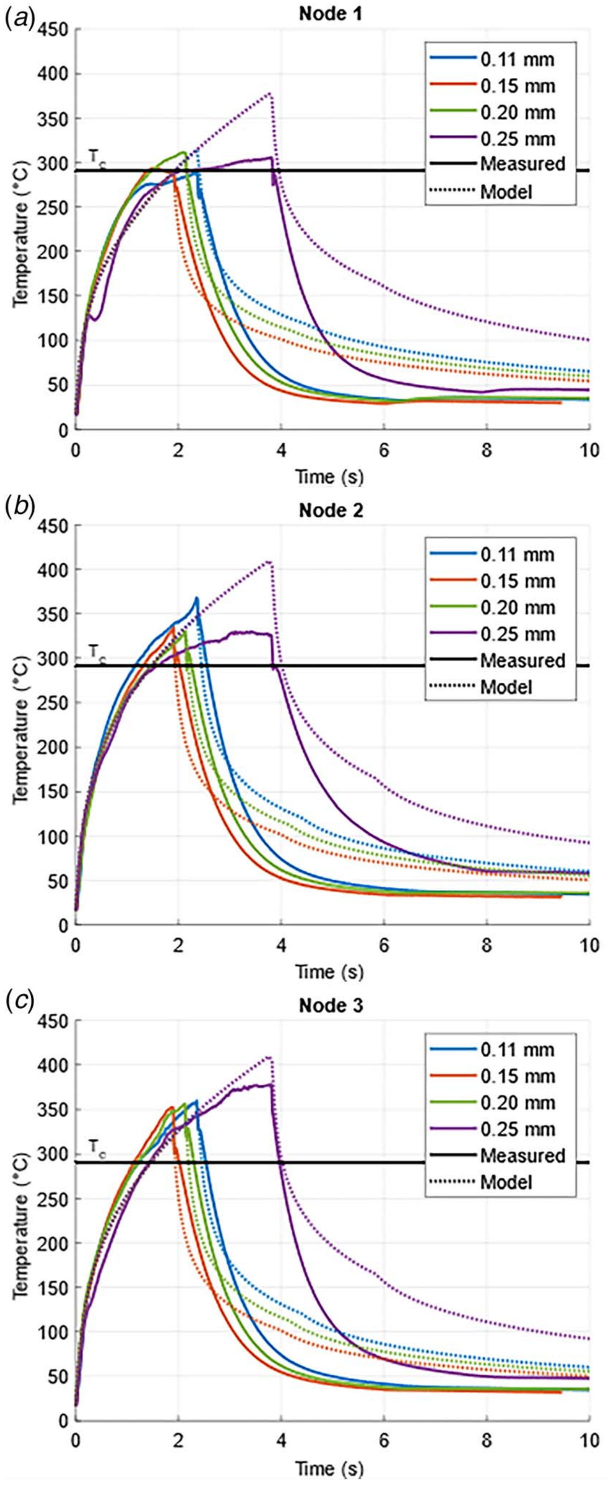

Fig. 8 Representative temperature profiles for travel-control trials (trials 1–4 in Table 3) at (*a*) node 1, (*b*) node 2, and (*c*) node 3 (shown in Fig. 2). The horizontal lines represent melting temperature (T_c) of the PPS matrix.

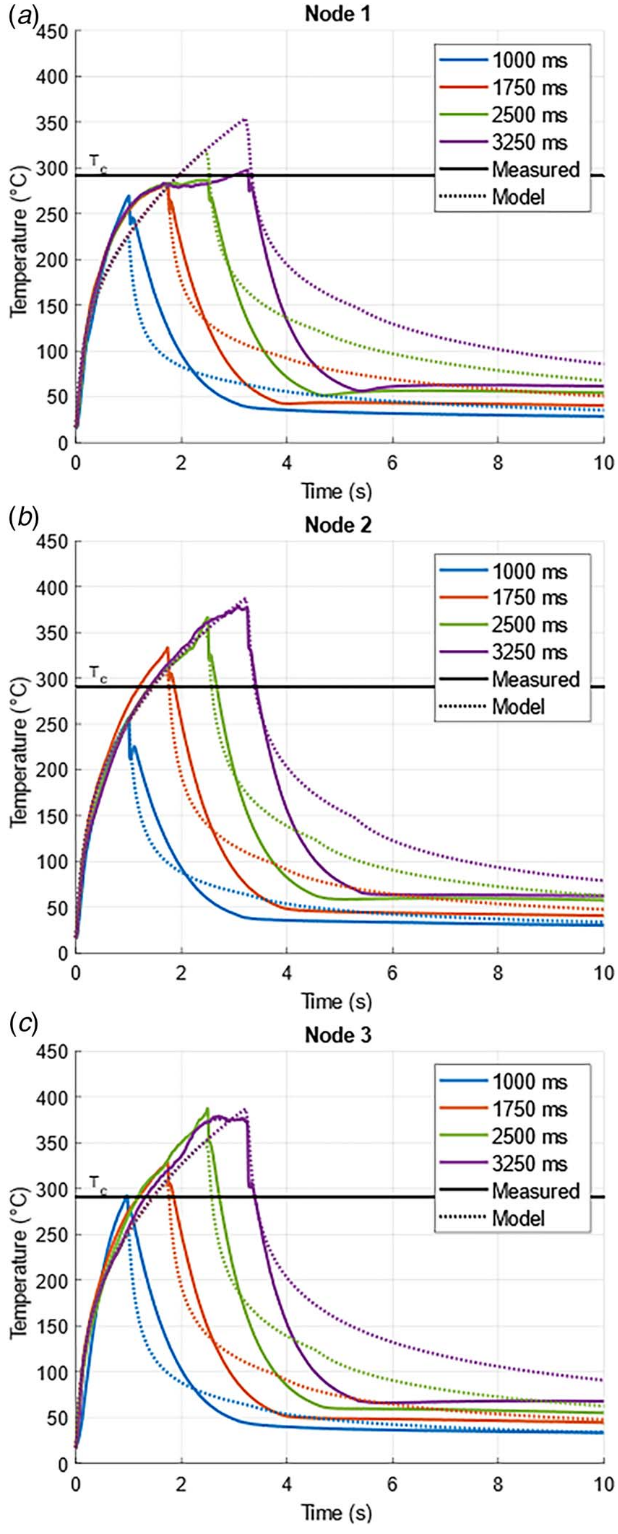

Fig. 9 Representative temperature profiles for time-control trials (trials 5–8 in Table 3) at (*a*) node 1, (*b*) node 2, and (*c*) node 3 (shown in Fig. 2). The horizontal lines represent melting temperature of the PPS matrix.

by unavoidable thermocouple movement and/or polymer flow over the thermocouple tip during compaction, resulting from the highest travel value (corresponding to the most significant polymer flow). Furthermore, it can be observed that node 2 and node 3 do not exhibit symmetry in their experimental temperature profiles, suggesting minor misalignment between the sonotrode and the platform.

Similar observations can be made for the results of the time-control trials (trials 5–8 in Table 3), as seen in Fig. 9. Good agreement between experiments and simulations is observed for node 2 and node 3 in the heating phase until peak temperature, while thermocouple measurements at node 1 for the two longest weld times displayed similar differences as observed in Figs. 8(*a*) and 8(*b*). As previously observed for travel-controlled trials, this is likely experimental error, caused by unavoidable thermocouple

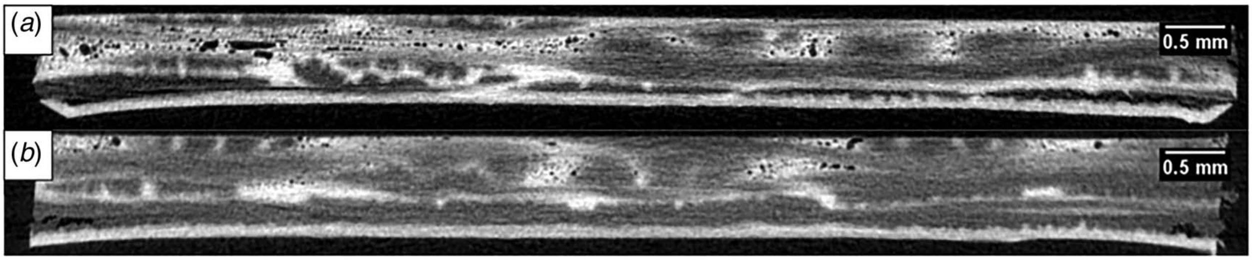

Fig. 10 Representative µCT slices for CF/PPS samples consolidated under (*a*) 0.15 mm travel and (*b*) 0.25 mm travel

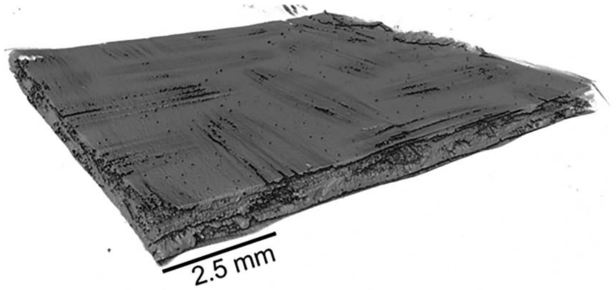

Fig. 11 3D reconstruction of a low-quality 0.15 mm CF/PPS sample from µCT imaging

Table 4 Average void content for all travel-based and reference samples, comparing µCT imaging and optical microscopy methods

Sample travel/weld time	µCT imaging average void content (%)	Optical microscopy average void content (%)
0.11 mm/2386 ms	3.82 ± 1.84	3.88 ± 1.92
0.15 mm/1903 ms	6.41 ± 1.90	4.54 ± 1.45
0.20 mm/2147 ms	4.02 ± 1.32	3.27 ± 1.25
0.25 mm/3814 ms	2.43 ± 0.81	2.57 ± 0.75
Compression molded (reference)		1.68 ± 0.61

misalignment and/or movement during polymer flow and compaction.

In general, the model adequately predicted the heating behavior for each case, and peak temperature (or heating cutoff) was determined by the weld time. On the other hand, the predicted cooling behavior for all cases generally showed good agreement for temperatures above the melting point, but deviated from the experimental profiles over time. The cooling rate for all samples in the FE model was lower than the experimentally measured cooling (ranging from approximately 70 °C/s to 108 °C/s, as calculated in the initial linear region of the cooling phase). A likely contributing factor for this discrepancy is that the model does not account for the flow of matrix material throughout consolidation. The sample may experience enhanced cooling due to the convective effects of viscous flow within the molten matrix during the solidification phase.

4.2 Microstructure of Consolidated Samples. Figure 10 shows representative µCT cross sections for travel-based samples (trials 1–4 in Table 3): 0.15 mm travel (Fig. 10(*a*)) and 0.25 mm travel (Fig. 10(*b*)). Figure 11 illustrates a full 3D reconstruction from µCT imaging for one of the worst-case trials (0.15 mm travel). Voids within the resin-rich areas (lighter-colored PPS matrix) were generally concentrated toward the top of the samples (closer to the sonotrode interface), likely due to air

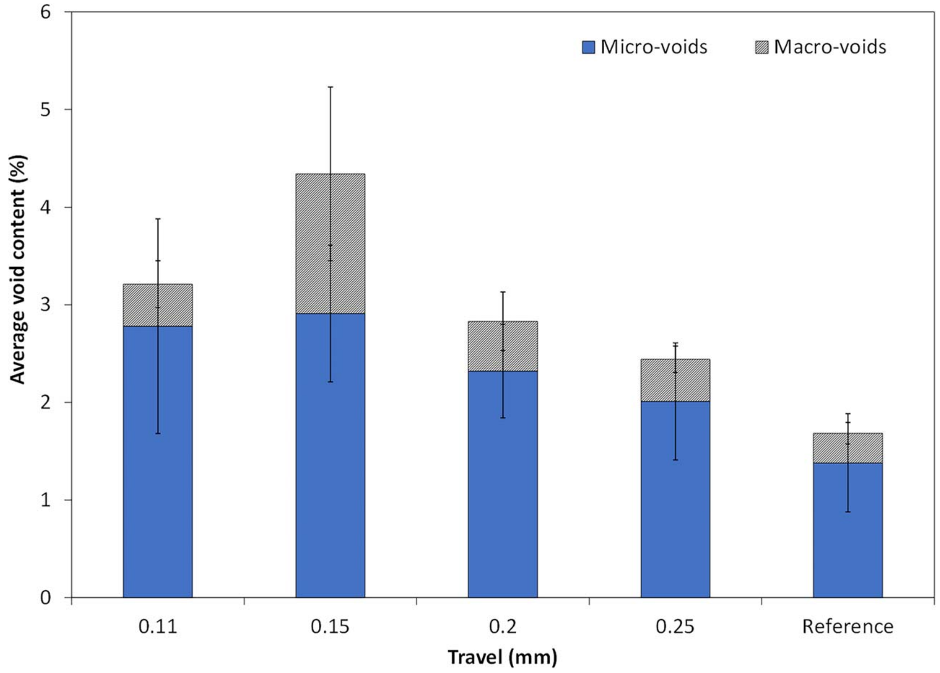

Fig. 12 Comparison between micro- and macro-void content obtained from optical microscopy image analysis

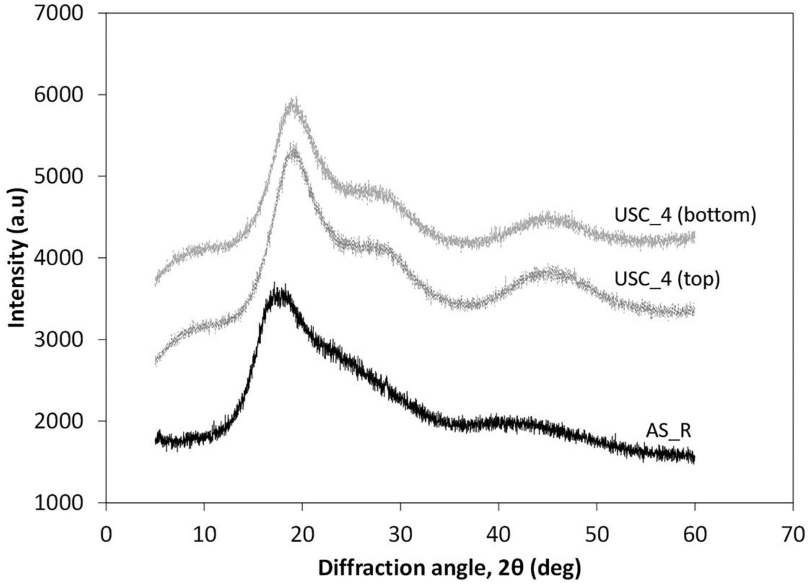

Fig. 13 XRD patterns for PPS films: as received (AS_R) and after USC on four layers (USC_4) on the top and bottom surfaces (1000 N welding force, 38.1 μm amplitude, and 0.20 mm travel). The patterns were shifted on the vertical axis for clarity.

bubbles moving to the surface of the molten PPS during polymer flow. In some cases, the bottom film did not fully melt, indicating it was not sufficiently heated to facilitate flow, as seen at the bottom of Fig. 10.

Table 4 summarizes the average void content for all travel-based trials, comparing μCT imaging and cross-sectional optical microscopy. Both analysis methods led to similar trends with respect to travel/weld time. The 0.25 mm samples exhibited the lowest estimated void content (2.43% and 2.57%), with the lowest standard deviation (0.81% and 0.75%). Conversely, the 0.15 mm samples had the highest estimated void content (6.41% and 4.54%). The welder outputs in Table 3 indicate that the weld time for the 0.15 mm trials was the lowest. It is also clear from the nodal temperature plots in Fig. 8 that the 0.15 mm specimen remained above the melting temperature for the smallest amount of time compared to other trials. This information suggests that the high void content in the 0.15 mm samples was likely due to insufficient time allowed for polymer flow, preventing air from migrating and escaping before re-solidification took place. By the same logic, the PPS matrix of the 0.25 mm sample spent the longest amount of time in the melted phase, allowing sufficient flow and more air bubbles to move out of the plies before the cooling phase began. Overall, it is possible to reach void contents below 4% through USC for woven specimens, similarly to what was measured for unidirectional rovings [15]. Compression molded specimens, as described in Sec. 2.3, were used as a comparison with the USC method. Void content was estimated as $1.68 \pm 0.61\%$ through cross-sectional optical microscopy. While generally lower than USC samples, 0.25 mm travel input achieved an average void content within standard deviation. Moreover, for CF/PPS, it was also shown in the literature that void content values above 2.8% could lead to a noticeable decrease in mechanical properties [21]. Micro- and macro-void contents (inside fiber tows and between plies) were estimated from optical microscopy images, as shown in Fig. 12. This confirms that micro-voids are dominant for both USC samples and the reference samples (compression molded). That being said, the overall void contents are consistent with averages found in previous ultrasonically consolidated woven CF/PPS samples [17].

4.3 Crystalline Structure Characterization. During USC, it was experimentally observed that there was a small temperature gradient through-the-thickness (Fig. 8, between node 1 and nodes 2–3). Moreover, the transparency of the PPS matrix varied from inner consolidated area to outer unconsolidated area (see Fig. 3). It was therefore hypothesized that the process could influence the crystalline structure of the matrix, especially given the fast cooling rates and small through-thickness temperature gradient. Wide-angle XRD patterns are presented in Fig. 13 for PPS films under various post-treatment conditions: AS_R (as received PPS film without any modification or treatment) and USC_4 (four layers of PPS films ultrasonically consolidated like CF/PPS samples, on top and bottom surfaces).

All PPS samples show a mostly amorphous structure with broad peaks at 19.2 deg, related to overlapping peaks of (110), (102), (200), and (111) crystalline planes [33,34]. For the USC_4 samples, the XRD patterns are similar for top and bottom surfaces, which indicates that the layers were evenly affected through the thickness. In particular, the USC_4 diffractograms with sharper peaks in the $19.2\ \text{deg} < 2\theta < 25\ \text{deg}$ range are comparable to what

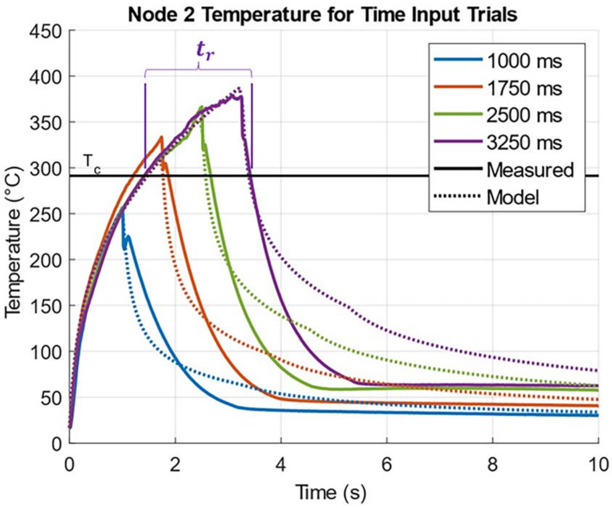

Fig. 14 Graphical depiction of residence time (t_r) for longest weld time at node 2 for time-control trials

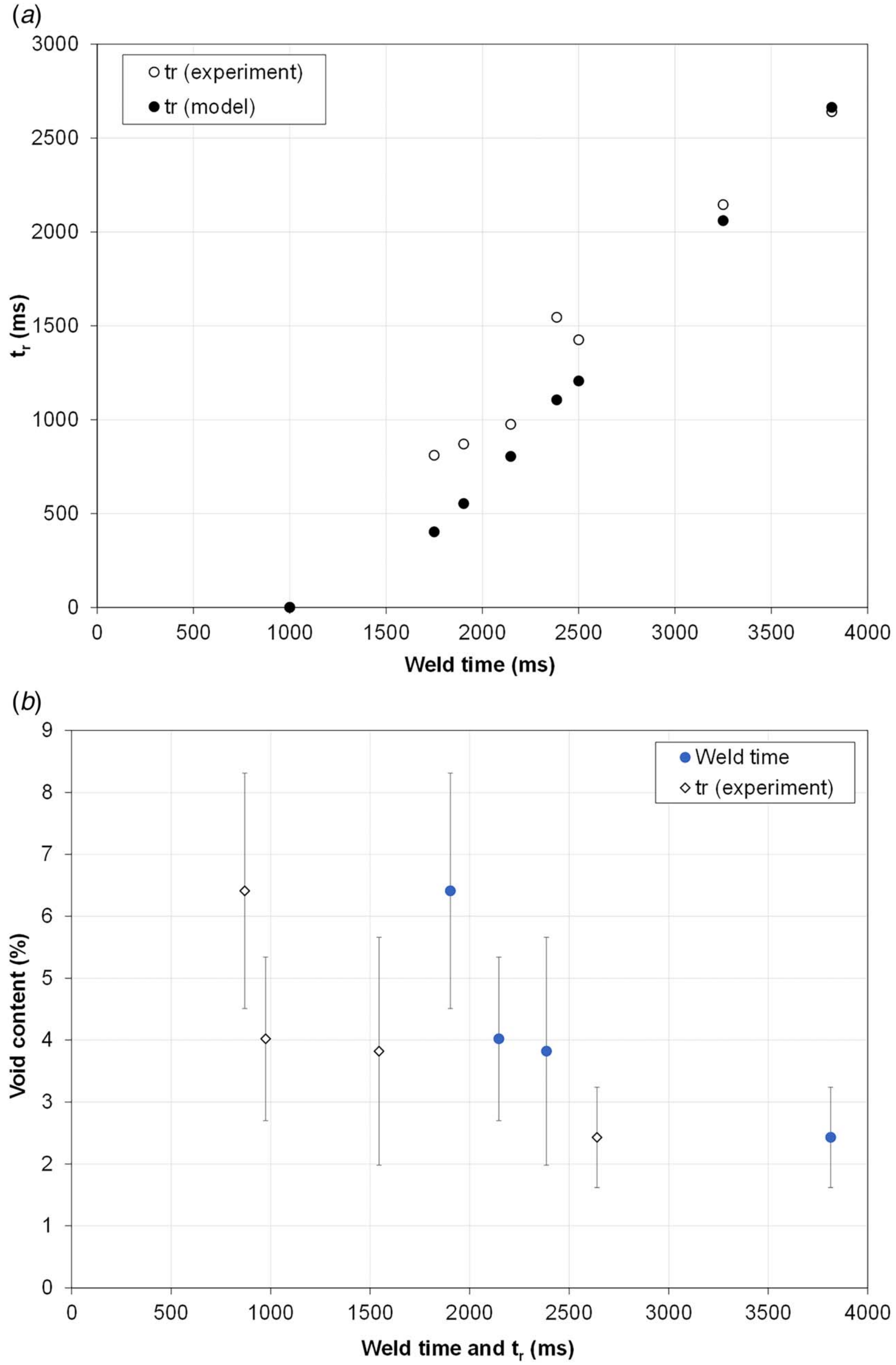

Fig. 15 (a) Comparison between experimental and simulated residence time (t_r) above melting temperature with respect to total weld time for travel- and time-control trials (representative data are shown for node 2) and (b) void content with respect to weld time and experimental residence time (t_r) for travel-control trials

was observed by Koutras et al. at the welded interface for PPS films used as energy directors under high force and amplitude conditions (1000 N and 86.2 μm) [19]. While XRD was also performed on CF/PPS specimens after USC on their top and bottom surfaces, the diffraction patterns only showed peaks consistent with carbon fiber (i.e., 25 deg and 44 deg corresponding to (002) and (011) planes, respectively [35]). For the consolidated samples, there were no visible peaks related to PPS, but the pattern for the bottom surface revealed a lower intensity, broader peak than the one for the top surface. It can be assumed that PPS was either amorphous or the low volume of PPS matrix could not diffract characteristic peaks with significant intensity.

4.4 Discussion.

This section will discuss two main topics: (1) how weld time and temperature profiles can be related to sample quality and (2) the effect of ultrasonic consolidation on crystallization behavior. As previously observed in Figs. 8 and 9, the simulated temperature profiles generated for each set of weld parameters generally showed good agreement with experimental data in the vibration phase. This study is concerned with relating temperature profiles (modeled and experimentally measured) to quality of the consolidated specimens. It can be inferred that the amount of time the melted matrix is allowed to flow within the sample is directly related to the extent of impregnation of the dry CF plies, and therefore, has a direct impact on the void content of the consolidated specimen. Thus, a parameter called residence time (t_r) was defined as the amount of time the PPS matrix spent above the melting temperature (T_c) at a given location in the material. Figure 14 illustrates the residence time, t_r, for node 2 at the longest weld time for time-controlled trials.

Comparison between the simulated and experimental residence time (t_r) above the melting temperature (T_c) at node 2 for travel control (Fig. 8(*b*)) and time-control (Fig. 9(*b*)) trials is shown in Fig. 15(*a*). In most cases, an error lower than 10% was estimated for travel- and time-control modes. Similar results were obtained for other node locations. This implies that the model can adequately predict the evolution of the matrix phase change and the amount of time the matrix remains in the melted state near the center of the sample (through-the-thickness), confirming the validity of the developed FE model. For all samples that underwent void content analysis, longer weld times (and subsequent extended periods of liquid-phase polymer flow of the matrix) yielded specimens with lower void content, as illustrated in Fig. 15(*b*) for μCT image analysis. The same trend was observed for optical microscopy samples, as seen in Table 4. When comparing weld time data from Table 3 with void content from Table 4, the latter generally decreased (from 6.41% to 2.43% or from 4.54% to 2.57%) with an increase in weld time (from approximately 1903 ms to 3814 ms). This corresponds to residence times above T_c from 870 ms to 2640 ms. A residence time above 2600 ms was sufficient to reduce macro-voids (between CF layers) and consolidate the layers, but micro-voids remained within the fiber tows (Fig. 12). The standard deviation for void content (Fig. 15(*b*) and Table 4) decreased with an increase in weld time. Lower weld times are associated with lower compaction and uniformity as the PPS matrix did not have sufficient time to flow within and between all tows. At higher weld times, samples were more uniformly compacted, therefore leading to lower variability. Nevertheless, the model presented in this manuscript can be used to reasonably estimate process parameters as it allows prediction of the residence time for a given polymer matrix, according to weld time used to control the consolidation process.

Regarding the effect of ultrasonic consolidation on crystallization behavior, limited data available in the literature indicate that fast cooling rates led to mostly amorphous PPS matrix (Fig. 13), but strain-induced crystallization (SIC) could also take place, as suggested through previous work [17] and by Koutras et al. [18]. The average crystallite size of the crystalline phase of PPS, D, can be calculated based on the Scherrer equation, Eq. (18):

$$D = \frac{K\lambda}{(B\cos\theta)} \tag{18}$$

where K is a shape factor, approximated as 0.9 [36], λ is the wavelength of the X-rays (CuKα radiation with $\lambda = 1.540598$ Å), B is the full-width at the half maximum intensity of the diffraction peak, and θ is the Bragg angle. The average crystallite size of the crystalline phase was estimated as 17.8 Å (AS_R), 23.7 Å (USC_4 top), and 24.3 Å (USC_4 bottom). As mentioned in Sec. 4.3, the broad peaks indicate a mostly amorphous structure. Those values are similar to PPS films after ultrasonic welding of CF/PPS single lap joints under high force and amplitude conditions, corresponding to a crystallinity between 2% and 3% [19]. The high cooling rates after the USC process (70 °C/s to 108 °C/s) induced a low degree of crystallinity as more time would be needed for polymer chains to reorganize into crystallites. To further increase crystallinity of ultrasonically consolidated samples, annealing (>120 °C) and the effect of welding force on SIC should be considered.

5 Conclusion

In this study, USC of dry CF plies with high-temperature PPS films was investigated with respect to two main objectives: (1) develop a simplified FE model to predict cross-sectional temperature profile providing guidelines for experimental parameters selection (i.e., weld time) and (2) further understand the effect of ultrasonic parameters on micro-structural quality based on thermal history. To this end, a 2D finite element model was implemented to compute the temperature distribution in layered CF/PPS thermoplastic composites during ultrasonic consolidation. The model took into consideration melting behavior of the PPS matrix, viscoelastic heat generation, and control of the process through time or travel (vertical displacement of the sonotrode). Comparison with experimental results showed that it can adequately predict temperature profiles and assist with process control through the weld time and residence time spent above the melting temperature.

In particular, it was desirable to determine the time at which the PPS matrix exceeded the melting temperature to ensure polymer flow and fabric impregnation, which resulted in better consolidation and lower void content. It was found that welding time values below 1750 ms were insufficient to reach melting temperature, whereas time above 3000 ms led to the lowest average void content (2.43 ± 0.81%), corresponding to a residence time above 2600 ms. XRD characterization revealed that the USC process led to mostly amorphous PPS, due to the high cooling rates (70 °C/s to 108 °C/s).

Overall, the thermal and micro-structural outcomes confirmed the feasibility of the USC process for layered composites made from dry fabric plies and high-temperature thermoplastic films. Future work to improve both experimental (lower void content) and simulation outcomes encompasses the following: (1) assessment of maximum thickness and size limits, (2) effect of post-consolidation force on sample quality, and (3) model improvements regarding cyclic amplitude implementation, frictional heating effects, and cooling phase.

Acknowledgment

This work was supported by the National Science Foundation (NSF) CAREER award (CMMI, Advanced Manufacturing, Award #2045955) and the Louisiana Board of Regents under the Research Competitiveness Subprogram (contract number LEQSF (2018–2023)-RD-A-05). The authors gratefully acknowledge Dr. Michelle Osborne, from the LSU School of Veterinary Medicine, for her assistance with μCT scans.

Conflict of Interest

There are no conflicts of interest.

Data Availability Statement

The datasets generated and supporting the findings of this article are obtainable from the corresponding author upon reasonable request.

References

[1] Yousefpour, A., Hojjati, M., and Immarigeon, J.-P., 2004, "Fusion Bonding/Welding of Thermoplastic Composites," J. Thermoplast. Compos. Mater., **17**(4), pp. 303–341.

[2] Zhi, Q., Tan, X.-R., Lu, L., Chen, L.-Y., Li, J.-C., and Liu, Z.-X., 2017, "Decomposition of Ultrasonically Welded Carbon Fiber/Polyamide 66 and Its Effect on Weld Quality," Weld. World, **61**(5), pp. 1017–1028.

[3] Yang, Y., Li, Y., Liu, Z., Li, Y., Ao, S., and Luo, Z., 2022, "Ultrasonic Welding of Short Carbon Fiber Reinforced PEEK With Spherical Surface Anvils," Compos. B Eng., **231**, p. 109599.

[4] Wang, K., Wang, X., Yi, M., Li, Y., and Li, J., 2022, "Investigation of Ultrasonically Welded Thermoplastic Composite Joints Using Netlike Energy Directors," ASME J. Manuf. Sci. Eng., **144**(5), p. 051004.

[5] Villegas, I. F., 2015, "In Situ Monitoring of Ultrasonic Welding of Thermoplastic Composites Through Power and Displacement Data," J. Thermoplast. Compos. Mater., **28**(1), pp. 66–85.

[6] Bhudolia, S. K., Gohel, G., Leong, K. F., and Barsotti, R. J., 2020, "Investigation on Ultrasonic Welding Attributes of Novel Carbon/Elium® Composites," Materials, **13**(5), p. 1117.

[7] Jongbloed, B., Teuwen, J., Palardy, G., Fernandez Villegas, I., and Benedictus, R., 2020, "Continuous Ultrasonic Welding of Thermoplastic Composites: Enhancing the Weld Uniformity by Changing the Energy Director," J. Compos. Mater., **54**(15), pp. 2023–2035.

[8] Engelschall, M., Larsen, L., Fischer, F., and Kupke, M., "Robot-Based Continuous Ultrasonic Welding for Automated Production of Aerospace Structures," Proc. SAMPE Europe, Nantes, France, Sept. 17–19.

[9] Yang, Y., Liu, Z., Wang, Y., and Li, Y., 2022, "Numerical Study of Contact Behavior and Temperature Characterization in Ultrasonic Welding of CF/PA66," Polymers, **14**(4), p. 683.

[10] Takamura, M., Uehara, K., Koyanagi, J., and Takeda, S., 2021, "Multi-Timescale Simulations of Temperature Elevation for Ultrasonic Welding of CFRP With Energy Director," J. Multiscale Model., **12**(4), p. 2143003.

[11] Rizzolo, R. H., and Walczyk, D. F., 2016, "Ultrasonic Consolidation of Thermoplastic Composite Prepreg for Automated Fiber Placement," J. Thermoplast. Compos. Mater., **29**(11), pp. 1480–1497.

[12] Gomer, A., Zou, W., Grigat, N., Sackmann, J., and Schomburg, W., 2018, "Fabrication of Fiber Reinforced Plastics by Ultrasonic Welding," J. Compos. Sci., **2**(3), p. 56.

[13] Lionetto, F., Dell'Anna, R., Montagna, F., and Maffezzoli, A., 2016, "Modeling of Continuous Ultrasonic Impregnation and Consolidation of Thermoplastic Matrix Composites," Compos. Part A Appl. Sci. Manuf., **82**, pp. 119–129.

[14] Lionetto, F., Dell'Anna, R., Montagna, F., and Maffezzoli, A., 2015, "Ultrasonic Assisted Consolidation of Commingled Thermoplastic/Glass Fiber Rovings," Front. Mater., **2**, p. 32.

[15] Dell'Anna, R., Lionetto, F., Montagna, F., and Maffezzoli, A., 2018, "Lay-Up and Consolidation of a Composite Pipe by In Situ Ultrasonic Welding of a Thermoplastic Matrix Composite Tape," Materials (Basel), **11**(5), p. 786.

[16] Mehdikhani, M., Gorbatikh, L., Verpoest, I., and Lomov, S. V., 2019, "Voids in Fiber-Reinforced Polymer Composites: A Review on Their Formation, Characteristics, and Effects on Mechanical Performance," J. Compos. Mater., **53**(12), pp. 1579–1669.

[17] Williams, S., and Palardy, G., 2020, "Ultrasonic Consolidation of Dry Carbon Fiber and Polyphenylene Sulfide Film," SAMPE Virtual Series, Virtual, July 17.

[18] Koutras, N., Benedictus, R., and Villegas, I. F., 2021, "Thermal Effects on the Performance of Ultrasonically Welded CF/PPS Joints and Its Correlation to the Degree of Crystallinity at the Weldline," Compos. Part C: Open Access, **4**, p. 100093.

[19] Koutras, N., Amirdine, J., Boyard, N., Fernandez Villegas, I., and Benedictus, R., 2019, "Characterisation of Crystallinity at the Interface of Ultrasonically Welded Carbon Fibre PPS Joints," Compos. Part A: Appl. Sci. Manuf., **125**, p. 105574.

[20] Agarwal, B. D., Broutman, L. J., and Chandrashekhara, K., 2018, *Analysis and Performance of Fiber Composites*, John Wiley & Sons, Inc., Hoboken, NJ.

[21] Liu, D., Zhu, Y., Ding, J., Lin, X., and Fan, X., 2015, "Experimental Investigation of Carbon Fiber Reinforced Poly(Phenylene Sulfide) Composites Prepared Using a Double-Belt Press," Compos. B Eng., **77**, pp. 363–370.

[22] Benatar, A., and Cheng, Z., 1989, "Ultrasonic Welding of Thermoplastics in the Far-Field," Polym. Eng. Sci., **29**(23), pp. 1699–1704.

[23] Levy, A., Le Corre, S., and Fernandez Villegas, I., 2014, "Modeling of the Heating Phenomena in Ultrasonic Welding of Thermoplastic Composites With Flat Energy Directors," J. Mater. Process. Technol., **214**(7), pp. 1361–1371.

[24] Villegas, I. F., 2014, "Strength Development Versus Process Data in Ultrasonic Welding of Thermoplastic Composites With Flat Energy Directors and Its Application to the Definition of Optimum Processing Parameters," Compos. Part A Appl. Sci. Manuf., **65**, pp. 27–37.

[25] B. G. Brito, C., Teuwen, J., Dransfeld, C. A., and F. Villegas, I., 2022, "The Effects of Misaligned Adherends on Static Ultrasonic Welding of Thermoplastic Composites," Compos. Part A Appl. Sci. Manuf., **155**, p. 106810.

[26] Tateishi, N., North, T. H., and Woodhams, R. T., 1992, "Ultrasonic Welding Using Tie-Layer Materials. Part I: Analysis of Process Operation," Polym. Eng. Sci., **32**(9), pp. 600–611.

[27] Greco, A., and Maffezzoli, A., 2003, "Statistical and Kinetic Approaches for Linear Low-Density Polyethylene Melting Modeling," J. Appl. Polym. Sci., **89**(2), pp. 289–295.

[28] Tsoularis, A. N., and Wallace, J., 2002, "Analysis of Logistic Growth Models," Math. Biosci., **179**(1), pp. 21–55.

[29] Seber, G. A. F., and Wild, C. J., 1989, *Nonlinear Regression*, John Wiley & Sons, Nashville, TN.

[30] Cao, L., Shi, P.-J., Li, L., and Chen, G., 2019, "A New Flexible Sigmoidal Growth Model," Symmetry, **11**(2), p. 204.

[31] Roylance, M., Player, J., Zukas, W., and Roylance, D., 2004, "Modeling of Ultrasonic Processing," J. Appl. Polym. Sci., **93**(4), pp. 1609–1615.

[32] Hoskins, D., and Palardy, G., 2020, "High-Speed Consolidation and Repair of Carbon Fiber/Epoxy Laminates Through Ultrasonic Vibrations: A Feasibility Study," J. Compos. Mater., **54**(20), pp. 2707–2721.

[33] Hu, Z., Li, L., Sun, B., Meng, S., Chen, L., and Zhu, M., 2015, "Effect of TiO_2@SiO_2 Nanoparticles on the Mechanical and UV-Resistance Properties of Polyphenylene Sulfide Fibers," Prog. Nat. Sci.: Mater. Int., **25**(4), pp. 310–315.

[34] Zhang, M., Wang, X., Bai, Y., Li, Z., and Cheng, B., 2017, "C60 as Fine Fillers to Improve Poly(Phenylene Sulfide) Electrical Conductivity and Mechanical Property," Sci. Rep., **7**(1), p. 4443.

[35] Amaral, M. A. D., Matsushima, J. T., Rezende, M. C., Gonçalves, E. S., Marcuzzo, J. S., and Baldan, M. R., 2017, "Production and Characterization of Activated Carbon Fiber From Textile PAN Fiber," J. Aerosp. Technol. Manage., **9**(4), pp. 423–430.

[36] Lee, T. H., Boey, F. Y. C., and Khor, K. A., 1995, "X-Ray Diffraction Analysis Technique for Determining the Polymer Crystallinity in a Polyphenylene Sulfide Composite," Polym. Compos., **16**(6), pp. 481–488.